GEOPHYSICS, VOL. 77, NO. 3 (MAY-JUNE 2012); P. KS1–KS12, 10 FIGS., 1 TABLE.
10.1190/GEO2011-0032.1

Integration of hydraulically induced microseismic event locations with active seismic attributes: A North Texas Barnett Shale case study

Xavier E. Refunjol[1], Katie M. Keranen[2], Joël H. Le Calvez[3], and Kurt J. Marfurt[2]

ABSTRACT

Hydraulic fractures are delineated by induced microseismic event distributions and typically propagate perpendicular to the regional minimum stress direction. However, at a smaller scale, varying mineralogical composition and existing fault and fracture networks can influence developing fracture networks. We integrated microseismic event locations with seismic attributes from multichannel seismic reflection data, including inversion results for impedance and Lamé parameters, and seismic curvature attributes. We found that microseismic event locations consistently correlate to zones of low seismic impedance and low $\lambda\rho$ and $\mu\rho$ values, describing characteristic material properties of fracture-prone zones within the North Texas Lower and Upper Barnett Shale. Additionally, event locations showed a weak correlation with anticlinal structures as defined by volumetric curvature attributes. We suggest that the low impedance, low $\lambda\rho$ and $\mu\rho$ zones were related to the boundary between calcite-filled fractures and the host rock.

INTRODUCTION

The generation of drainage pathways during hydraulic stimulation within a volume of rock can be monitored by recording and locating induced microseismicity. The microseismicity is assumed to occur along, and thus delineate, the developing fractures or reactivated fracture networks. However, predictions of the locations and orientations of induced fracture pathways based on the orientation of maximum horizontal stress (e.g., Rich et al., 2010) are not sufficient to characterize the complexity of fracture networks. Though induced fracture networks develop in accordance with the stress orientations at the macroscale, the actual locations of fractures are more challenging to predict. Hydraulic fracture propagation is time-dependent, and fractures follow the path of least resistance (Economides and Martin, 2007), and hence, factors in addition to the regional stress field can influence rock failure. These factors include the variability in the local stress field, formation anisotropy, and heterogeneous mineralogical composition. These factors often result in variable fracture gradients and fracture zones (Jarvie et al., 2007). The variability in the developed fracture networks increases the risk of fracturing nonhydrocarbon-rich zones, including water-bearing formations.

Here, we characterize rock properties within a seismic volume from the North Texas Barnett Shale and correlate the properties with locations of microseismic events. We provide ranges of seismic properties from regions of the active seismic data that were preferentially fractured during stimulation, and suggest that these properties delineate zones that will preferentially fracture during future stimulations within similar gas-rich shale units.

We use a seismic data set from a 14-square-mile seismic survey in Tarrant County targeting the Barnett Shale within the Fort Worth basin (Figure 1). Using prestack seismic data from this survey, we generate seismic inversion volumes including volumes of P- and S-impedance and Lamé parameters. In the seismic inversion we jointly invert the seismic data with density, shear, and compressional velocity logs acquired in wells within the survey area. We also generate volumetric curvature volumes from poststack seismic data from the survey.

Our results characterize the matrix properties of the subset of the Barnett Shale demonstrated to be the most likely to fail. Failure indicated by locations of microseismic events, occurs in zones that are preferentially of low acoustic and shear seismic impedance. Our results also suggest a weak correlation between the locations of microseismic events and seismic curvature attributes. We suggest that active-source seismic reflection data can characterize the properties of rocks most likely to fail during hydraulic fracturing.

Manuscript received by the Editor 16 February 2011; revised manuscript received 9 October 2011; published online 20 April 2012.
[1]The University of Oklahoma and Swift Energy, Norman, Oklahoma, USA. E-mail: xavier.refunjol@swiftenergy.com.
[2]The University of Oklahoma, Norman, Oklahoma, USA. E-mail: keranen@ou.edu; kmarfurt@ou.edu.
[3]Schlumberger, Houston, Texas, USA. E-mail: jcalvez2@slb.com.

BACKGROUND

Geologic background

The Barnett Shale is the primary source rock for Paleozoic hydrocarbon production in the Bend Arch–Fort Worth Basin area (Pollastro et al., 2007). The shale is a high-thermal-maturity gas-shale system that generates, retains, and stores hydrocarbons (Jarvie et al., 2007). The Barnett Shale is a calcite-rich shale with high biogenic silica content, clay to silt-sized calcite, and dolomite and calcite-dominated skeletal debris (Jarvie et al., 2007; Loucks and Ruppel, 2007). The Fort Worth Basin covers roughly 15,000 mi^2 in north-central Texas, and deepens toward the north with an axis roughly paralleling the Muenster Arch, a basement uplift with a northwest–southeast trend (Figure 1) (Pollastro et al., 2007). The basin is bounded on the north by the Muenster Arch and the Red River basement uplift. A major fault, the Mineral Wells Fault, crosses the northeastern portion of the basin with a northeast–southwest trend. The Mineral Wells Fault is subparallel to the trend of the Ouachita thrust on the southern margin of the Forth Worth Basin (Pollastro et al., 2007).

Within the Fort Worth Basin, the Barnett Shale is deposited above the Ordovician unconformity, on either the Ellenburger Group or the Viola Limestone/Simpson group. It is separated into the Upper and Lower Barnett Shale units by the Forestburg Limestone in areas, and is overlain by the Upper Barnett Limestone and the Marble Falls Limestone.

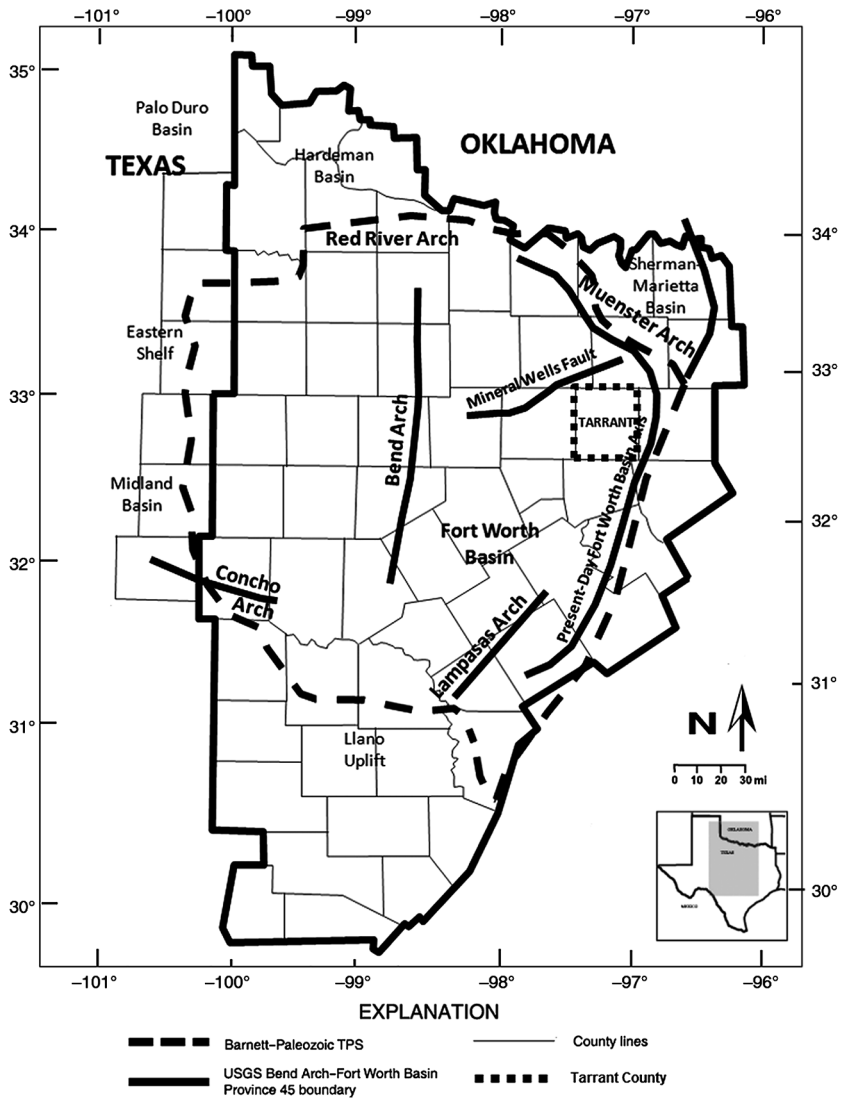

Figure 1. Map of the Bend-Arch Fort Worth Basin depicting the major structures and the Tarrant County study area (modified from Pollastro et al., 2007). TPS: total petroleum system, including source, reservoir, and traps.

Fracture propagation

Shale reservoirs have low values of matrix porosity and permeability, including the Barnett Shale formation. Hydraulic stimulation creates rough fracture surfaces and permeability by opening natural fractures or creating additional new fractures, improving reserve recovery for a given well (Rutledge and Phillips, 2003; Gale et al., 2007; Miskimins, 2009). In theory, induced fracture networks propagate perpendicularly to or nearly perpendicularly to the minimum horizontal stress $S_{H\,\mathrm{min}}$ and the fractures enhance permeability and drainage of the stimulated area. Nevertheless, the process of hydraulic fracturing is time dependent and fractures follow paths of least resistance (Economides and Martin, 2007), which are sensitive to local mineralogy and the local stress regime. The local stress regime may change during stimulation because of preceding fractures (Miskimins, 2009), complicating a priori assessments of where induced fractures will propagate.

Previous studies often assume that induced fractures preferentially propagate along preexisting fractures, considering the existing fractures to be planes of weakness (Zoback and Harjes, 1997; Shapiro et al., 2002; Rothert and Shapiro, 2003). However, recent studies have indicated that cement within fractures, if bound to the wall rock, may cause new hydraulic fractures to preferentially occur in previously unfractured rock (Thompson et al., 2010; Zhang et al., 2010). These studies included tight-gas sandstones with quartz cement filling fractures, whereas most existing fractures in the Barnett Shale are filled with carbonate cement (Gale et al., 2007; Jarvie et al. 2007; Pollastro et al., 2007). It is not known whether new fractures in the Barnett Shale preferentially reopen existing cemented fractures or create new fractures in unfractured rock. Gale et al. (2007) suggest that the calcite filling fractures within the Barnett Shale is not tightly bound to the wall rock, and that the tensile strength of the cement-wall contact is low. In this case, the cement fill may naturally part from the wall rock during hydraulic fracturing (Gale et al., 2007).

DATA

The seismic volumes used in this investigation cover 14.2 mi^2 in Tarrant County, Texas. Four

vibroseis sources used ten sweeps of 8 s each, with a frequency range of 10–110 Hz. The source interval was 95 m and the receiver interval was 67 m. The recording was carried out with a 2 ms sample rate, and processing used a CDP bin size of 34 by 34 m.

Microseismic data were collected from monitoring wells equipped with twelve downhole 3C (bandwidth of 3–1500 Hz) geophones to record events induced by the hydraulic fracture stimulation process. The geophones were placed at 11 m intervals, starting at the Marble Falls Limestone top and continuing to just above the Upper Barnett Shale. The microseismic event data set available for this study consists only of processed event locations.

METHODOLOGY

Seismic inversion

Induced fractures may develop within zones of similar mineralogical composition or strength, either along existing fractures or within unbroken formations. Therefore, locations of hydraulically induced microseismic fractures may correlate to rock properties including the density, acoustic impedance, and V_P/V_S ratio of the reservoir material. To analyze this relationship, we inverted measured seismic amplitudes from our 3D seismic data and measured seismic impedance from well-logs to produce an acoustic impedance volume. Our inversion result provides best-fit values of P-impedance, S-impedance, and density for each voxel within the volume. We will hereafter refer to this process as *seismic inversion*. The seismic inversion process we implemented follows a standard inversion scheme (Hampson and Russell, 2005) using the Hampson-Russell commercial software package.

Poststack seismic inversion is simpler and more economical than prestack seismic inversion, but has a noticeable disadvantage. The stacked traces are used in the poststack inversion as if they resulted from normal-incidence seismic rays; however, these are summed traces and contain effects of changing amplitudes as a function of offset. Impedance inversions using poststack volumes, therefore, do not represent the true reflectivity of the subsurface. Prestack inversion is able to account for the amplitude variations with offset, and consequently we used prestack data for our inversion.

The commercial model-based prestack inversion algorithm we used requires angle-dependent wavelets and angle stacks, and results in estimates of P-impedance (Z_P), S-impedance (Z_S), and density (ρ). This algorithm starts with an initial impedance model based on well-logs and interpreted seismic horizons, and updates the model in each iteration using the conjugate gradient method until the derived synthetic seismic section fits the observed seismic data to within a predefined misfit value (Hampson and Russell, 2005).

To check our results, we forward modeled the resulting P- and S-impedance volumes using Zoeppritz-based AVO equations to verify that predicted prestack seismic gathers closely match the recorded seismic data (e.g., Goffey, 2009). Three assumptions are made in the commercial algorithm used for this study: (1) the linearized approximation for reflectivity holds, (2) reflectivity as a function of angle can be approximated by the Aki-Richards equations (Aki and Richards, 2002), and (3) there is a linear relationship between P-impedance and S-impedance and density (Hampson and Russell, 2005).

Lamé parameters and fluid properties

We also use the generated P- and S-impedance volumes to calculate the Lamé parameters, incompressibility λ, and rigidity μ, for each voxel within our volume. Incompressibility is more sensitive to the pore fluids than to the rock matrix, and rigidity is sensitive to the matrix mineralogy and connectivity for elastic materials (Dufour et al., 2002). The Lamé parameters thus provide another tool to distinguish lithology and gas content, and appear more sensitive to these variations than seismic impedance (e.g., Goodway et al., 1997, 2010). Integrating the Lamé parameters with microseismic event locations provides additional characterization of the physical properties of zones that preferentially fail, and may possibly be used to assess the effectiveness of the stimulation program at fracturing the target gas-rich zone.

Lamé's parameters are:

$$\lambda\rho = Z_P^2 - 2Z_S^2, \tag{1}$$

and

$$\mu\rho = Z_S^2. \tag{2}$$

In past studies, crossplots of $\lambda\rho$ versus $\mu\rho$ (LMR) better differentiate lithologic properties and isolate gas zones than crossplots of Z_P versus Z_S (Goodway et al., 1997). In shale, low values of $\lambda\rho$, with values of $\lambda\rho < \mu\rho$, indicate brittle gas-rich shale zones (e.g., Goodway et al., 2010). Similarly in clastics, Aibaidula and McMechan (2009) and Goodway et al. (2010) observed decreasing $\lambda\rho$ with increasing gas content and porosity, along with decreasing shale content.

We utilize the Lamé parameter volumes we generate to analyze possible correlation between lithology and microseismic event locations, and to provide insight into the effectiveness of stimulations. The production history reflects the effects of both the development of an effective fracture network and the amount of hydrocarbons present (i.e., gas). By using the Lamé parameters as indicators of the amount of hydrocarbon present, we attempt to isolate the influence of the stimulation and developed fracture network on production history.

Curvature

Distinct from seismic inversion, which characterizes the seismic properties of subvolumes of rock that preferentially fracture, the complementary seismic-curvature attributes provide a method to image locations of preexisting fractures and faults (Lisle, 1994; Massaferro et al., 2003; Al-Dossary and Marfurt, 2006; Blumentritt et al., 2006). Folds and flexures, geometric shapes with high curvature, often host conjugate fault sets and fractures, creating a positive correlation between curvature attributes and fractured rock. Hydraulically induced microseismic events often occur within such fractured or faulted regions.

Curvature is a well-known seismic attribute defined at a particular point as the inverse of a circle's radius, where the circle is tangential to the surface at the given point (Roberts, 2001). This circle may lie below the plane and describe a positive curvature, or above the plane and describe a negative curvature. Maximum curvature, kmax, is the curvature of the tangent circle with the smallest radius.

Minimum curvature, kmin, is the curvature of the tangent circle perpendicular to the maximum curvature, kmax. For interpretation, the most-positive principal curvature, k_1, and most-negative principal curvature, k_2, are often used, where

$$k_1 = \mathrm{MAX}(\mathrm{kmax}, \mathrm{kmin}), \tag{3}$$

and,

$$k_2 = \mathrm{MIN}(\mathrm{kmax}, \mathrm{kmin}). \tag{4}$$

Relative values of k_1 and k_2 describe 3D quadratic shapes. The six basic shapes are the bowl, dome, ridge, valley, saddle, and plane (Figure 2). Here, we correlated the volumetric curvature attributes (Al-Dossary and Marfurt, 2006) to microseismic locations to investigate the correlation between properties of active seismic data and microseismic event locations. Volumetric curvature was preferred over surface curvature, as the latter will have an interpreter bias. Resolution is limited by the binning size and sampling of our surface seismic data set.

RESULTS

Seismic inversion

By combining our seismic inversion results with microseismic event locations, we can characterize the properties of materials preferentially fractured during hydraulic stimulation. We used a prestack unmigrated volume for our inversion, a reasonable selection because the Barnett Shale has a structural dip of less than 3° in our study area. Of the 274 wells drilled within the seismic survey boundaries, four wells have high-quality density and P-wave and S-wave velocity logs. The four wells used are located in the northern, central, and southern portions of the seismic volume, and are sufficiently well distributed to characterize the material properties within regions of the seismic survey. Although all four were used in our inversion, we primarily present results from two of these wells for brevity.

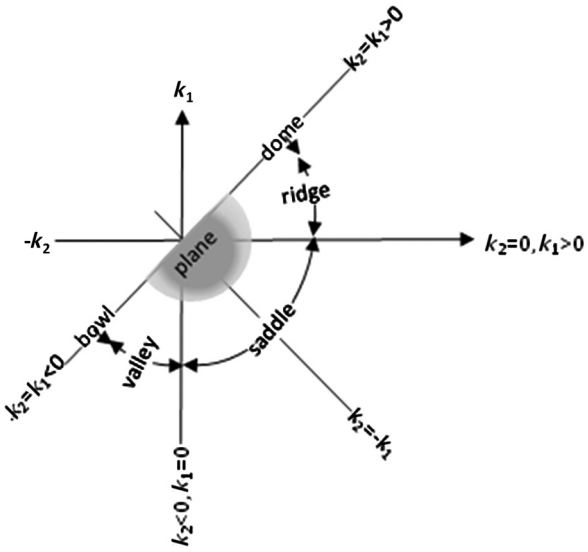

Figure 2. Diagram depicting the relationship between the different combinations of values of most-positive and most-negative principal curvatures, k_1 and k_2, and the six generated quadratic shapes; plane, dome, ridge, saddle, valley, and bowl. Locations with positive k_1 and k_2 values fall into the dome and ridge regions, locations with negative k_1 and k_2 values fall into the bowl and valley regions, regions with very low k_1 and k_2 values represent planes, and regions with k_1 and k_2 values of opposite sign represent saddles.

A low-frequency background model for the initial iteration of the inversion was constructed using curves from well logs filtered with a high-cut frequency of 10 Hz, tapered to 15 Hz, and extrapolated throughout the region using interpreted seismic horizons. Resulting wavelengths were approximately 381–405 m (1250–1330 ft) for shales and 466–530 m (1530–1740 ft) for limestones corresponding to the high-cut frequency, and wavelengths of 253–268 m (830–880 ft) for shales and 311–354 m (1020–1160 ft) for limestones corresponding to the tapered frequency. Well logs were frequency-filtered using the depth-to-time relationship established by our tie between the logs and surface seismic data.

To test the density, P-wave, and S-wave results of the impedance inversion, we extracted seismic wavelets from the seismic survey and created a synthetic seismic volume modeled from the inversion output (Figure 3). Near- (0°–15°) and mid-offset (15°–30°) zero-phase wavelets were extracted from subsets of the seismic volume from within the interval between the top of the Marble Falls Limestone formation and the bottom of the Lower Barnett Shale, between 1.1 to 1.4 s. From these wavelets and the inverted reflectivity model, we generated synthetic seismic traces between the Marble Falls formation and the Ordovician Unconformity using all wells within the data set. Figure 3 represents the resulting synthetic traces observed for all wells. A correlation of $R = 0.78$–0.94 was achieved between the recorded seismic gathers and the inverted synthetic gathers of near offsets within the target zone.

The average values of the inverted ρ, Z_P, Z_S, V_P/V_S ratio, $\lambda\rho$ and $\mu\rho$ within each formation are listed in Table 1. These values represent pixels 2 ms vertically by 33.5 m (110 ft) laterally. To account for possible interpretation bias, i.e., possibly incorrect identification of major seismic horizons, surfaces were also interpreted through the middle of the formations and values of each property were extracted and averaged over a range of ±5 ms on either side of the surface. These averaged results were consistent with the values extracted along the surface. The highest values of the inverted ρ, Z_P, Z_S, V_P/V_S, $\lambda\rho$ and $\mu\rho$ correspond to the Marble Falls and the Upper Barnett Limestone. These higher values are consistent with studies by Aibaidula and McMechan (2009), who found consistently lower density, impedance, and V_P/V_S ratios in shale formations than within the surrounding limestone formations. In our study, the inverted properties of the Upper and Lower Barnett Shale formations fall within the full range of properties of the Marble Falls and Upper Barnett Limestones, indicating similar composition. The Barnett Shale is a calcite-rich shale (Jarvie et al., 2007; Loucks and Ruppel, 2007). Inverted $\lambda\rho$ and $\mu\rho$ values have a pattern similar to the impedance values, as can be expected. The inverted Lamé parameters are consistent with values from Goodway et al. (1997); in our inversion $\lambda\rho$ is less than $\mu\rho$ for gas-rich zones.

ANALYSIS

Microseismic analysis and interpretation

Mapped microseismic events (Figure 4) reflect the basin's local and regional stress history. At the macroscale, events preferentially align parallel to the current maximum horizontal stress direction (northeast–southwest) (Heidbach et al., 2009), forming primary

northeast–southwest stress lineaments. We interpret that tectonic deformation throughout the basin's history created the observed primary fracture lineaments that parallel the Ouachita Thrust Front and the Mineral Wells Fault (Gale et al., 2007; Loucks and Ruppel, 2007; Pollastro et al., 2007). This is compatible with the concept that microseismicity associated with hydraulic fracturing is commonly triggered by small stress perturbations within naturally stressed, preexisting fractures (e.g., Zoback and Harjes, 1997; Shapiro et al., 2002).

Microseismic event clouds concentrate within individual formations. Wells B and C show dense microseismic event clouds in the lower Barnett Shale (73.56% of events) that lose intensity below the Ordovician Unconformity Viola surface (1.97% of events) (Figure 5). Similarly, event locations within the Lower Barnett Shale decrease in density within the Upper Barnett Shale (19.21% of events) at the high-calcite Forestburg Limestone, and the fracture system defined by microseismicity appears laterally extensive near the boundary. An event cloud within the Upper Barnett Limestone (3.57% of events) also appears to dissipate before reaching the denser Marble Falls Limestone (1.7% of events) (Figure 5). We note an apparent clustering on formation boundaries that may result from velocity jumps at the boundaries and corresponding processing artifacts. It is also possible, however, that some of these boundaries present barriers to fracture growth. For example, the Marble Falls Limestone above the Barnett Shale has a higher fracture threshold than the shale (Jarvie et al., 2007), possibly providing an upper barrier to stimulation. Additionally, though the higher density of microseismic events and the greater extent of the induced fracture system within the Lower Barnett Shale as compared to the Upper Barnett are controlled largely by targeted

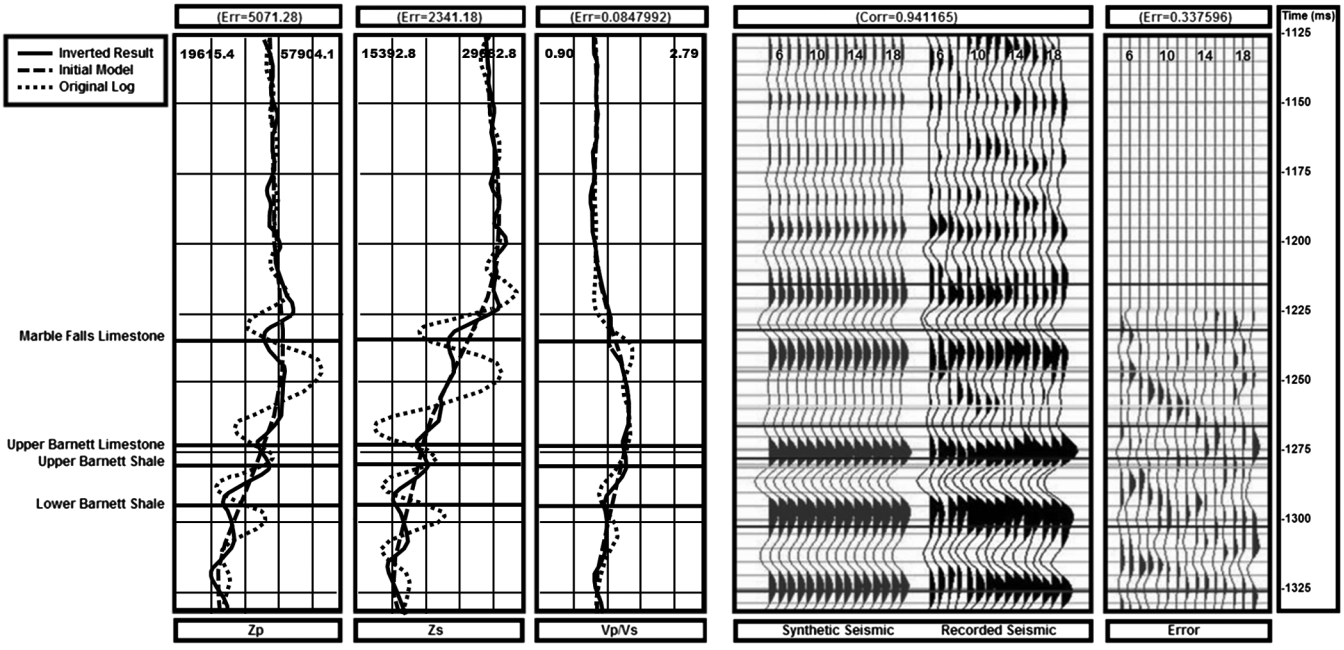

Figure 3. Comparison of the synthetic prestack seismic volume generated from inverted impedance with the recorded unmigrated seismic volume in the vicinity of wellbore D. Note that while the recorded seismic is unmigrated, there is a correlation of 0.94 and an uncertainty of 0.34 between the synthetic and recorded near and midangle gathers. The correlation is calculated only for the interval containing the reservoir rock and details in the overburden were not modeled.

Table 1. Average values of inverted properties: density, P- and S-impedance, V_P/V_S, λ_ρ and $\mu\rho$. Values were extracted from surfaces in the middle of each formation and averaged within a 10 ms window centered about each surface.

	ρ (g/cm^3)			Z_P (ft/s) $*$ (g/cm^3)			Z_S (ft/s) $*$ (g/cm^3)			V_P/V_S unitless			$\lambda\rho$ GPa $*$ (g/cm^3)			$\mu\rho$ GPa $*$ (g/cm^3)		
	Avg	Min	Max	Avg	Min	Max	Avg	Min	Max	Avg	Min	Max	Avg	Min	Max	Avg	Min	Max
M. Falls Ls.	2.64	2.60	2.68	40000	33000	46000	21500	19000	24000	1.88	1.68	2.04	62	30	100	42	30	55
U. Barnett Ls.	2.58	2.48	2.70	34000	27500	45500	20100	17500	23400	1.72	1.53	1.98	35	13	78	38	28	51
U. Barnett Sh.	2.52	2.43	2.61	32000	25000	37500	18800	16000	22000	1.66	1.46	1.80	24	4	46	34	24	48
L. Barnett Sh.	2.52	2.42	2.59	33000	25000	38000	19700	16200	22000	1.67	1.47	1.82	26	5	42	36	24	45

stimulation of the Lower Barnett, they may also be influenced by physical property differences. The Upper Barnett Shale has a higher fracture threshold than the less-dense Lower Barnett Shale, which has a higher clay content and fails at a lower stress (Jarvie et al., 2007; Loucks and Ruppel, 2007). The high silica and carbonate content of the Upper Barnett increases the density of the formation, observed in the well-log density curves and in our inversion results, and creates a higher fracture threshold than that of the Lower Barnett Shale, possibly hindering the development of fracture networks.

Microseismic location uncertainties

Uncertainties in the (commonly anisotropic) velocity model (Bardainne and Gaucher, 2010), acquisition geometry (Bulant et al., 2007), and picking of P- and S-wave arrivals in the presence of noise, are the general sources of uncertainty in microseismic event locations. Another source of uncertainty in downhole hydraulic monitoring is the possible misorientation of each 3C tool within the monitoring well.

Microseismic data sets recorded with downhole tools exhibit a distance-dependent uncertainty (location dispersion error), which causes systematic spreading of events as the distance between source and receiver increases (Warpinski, 2009; Eisner et al., 2010; Kidney et al., 2010). Moving away from the source also decreases recorded amplitudes by 1/distance through geometrical spreading, and thus lowers the signal-to-noise ratio (S/N). Vertical scattering uncertainty increases when short downhole sensor arrays are used, and when sensors are available only above true event locations. Downhole arrays with fewer sensors cause increased horizontal uncertainty and therefore, lateral dispersion error. Angular uncertainty for a vertical monitoring well decreases as $1/\sqrt{n}$, where n is equal the number of geophones (Warpinski, 2009). Eisner et al. (2010) and Kidney et al. (2010) find that the vertical uncertainty for a borehole single vertical array, such as the array used to acquire our data set, increases with distance from the borehole. At 152 m distance, vertical error can be on the order of 15 m, depending upon the velocity model and other parameters (Eisner et al., 2010; Kidney et al., 2010), but increases up to 46 m of vertical uncertainty at 610 m (Kidney et al., 2010). At 152 m distance, horizontal uncertainty is between 15 and 30 m, and increases to 60–107 m at a distance of 610 m (Eisner et al., 2010; Kidney et al., 2010).

Our microseismic data were acquired in 2003 and 2005, and processed prior to our study. Microseismic event locations in the full data set are at distances between 152 to 1067 m from the monitoring wells. Information on the uncertainty in event location was not provided; hence, we used a Monte Carlo analysis of 300 iterations at six different source locations within a velocity model to calculate approximate lateral and vertical location uncertainties for one well within our study area, albeit not one of the four wells with the full suite of well logs (e.g., Maxwell, 2009) (Figure 6). Standard deviations in uncertainty were calculated for each source location. We assumed that all 12 geophones recorded both P- and S-wave arrivals and that picking accuracy decreased by 1 ms for every 122 m of distance. Assuming that microseismic processing workflows were consistent and that seismic attenuation is constant within our region, this uncertainty analysis provides a reasonable representation of location uncertainties within our area. Azimuthal uncertainty results from the P-wave polarization analysis are shown in Figure 6, with two examples representing good (5°) and poor (10°) S/N of the P-wave. For these scenarios, vertical uncertainty ranges from 7.6 to 46 m, and horizontal uncertainty ranges from 6 to 107 m.

The cells of our seismic inversion are 2 ms (approximately 7.6 m, using a velocity of 3963 m/s) vertically, by 30 by 30 m. Therefore, events with location uncertainty less than or equal to these dimensions can be used with confidence to correlate event locations to seismic properties. However, as location uncertainty increases, the correlation between seismic inversion results and the microseismic event location is expected to decrease. We calculated the correlations between seismic properties and microseismic event locations for both the full microseismic data set and for only those events located within ~365 m of the monitoring well, a distance at which the uncertainty in microseismic event location is similar to the size of each inversion voxel.

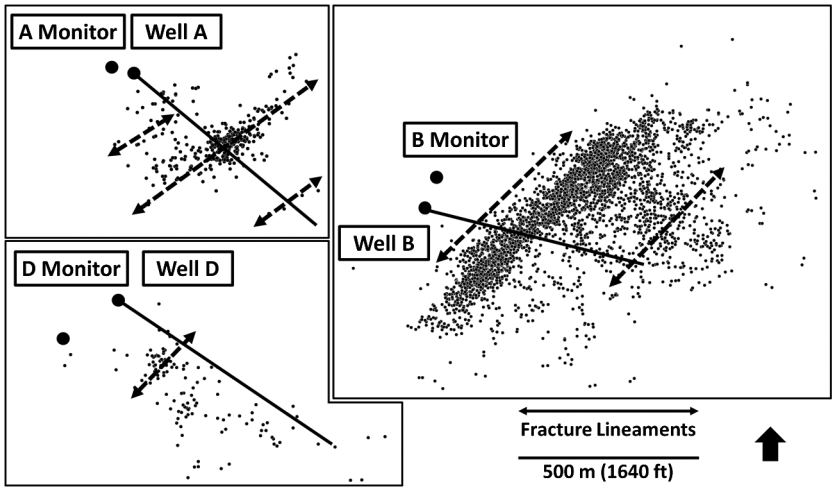

Figure 4. Mapped microseismic events of wells A, B, and D. The orientation of fracture lineaments formed by the microseismic clouds align parallel to the Ouachita thrust front and the Mineral Wells Fault.

Microseismic events and seismic inversion properties

By design of the hydraulic fracture job, the microseismic events occur primarily within the formation being stimulated; in this case, the Lower Barnett Shale. However, the mineralogical composition of the shale is highly variable, causing variable fracture gradients and complex fracture zones to develop (Jarvie et al., 2007). We integrated microseismic event locations with rock properties derived from surface seismic inversion volumes to examine their relationship and possible correlations.

We generated P- and S-impedance histograms for stimulated versus nonstimulated regions by using microseismic event locations to isolate impedance values from the volume of the stimulated area (Figure 7). Our results indicate that the microseismic events correspond to a specific range of inverted values for each property (density, impedance, etc.) in all stimulation stages of the studied wells, regardless of the

orientation or location of the wells. Fractures associated with hydraulic stimulation, represented by the microseismic locations, occur in lower impedance subvolumes of the fractured formations (approximately 65%–80%) near wells A and B (Figure 7). The same result is observed near wells C and D, but this is not included in the figure, for brevity. In all wells, microseismic events preferentially occur within the lowest impedance portions of the Barnett Shale (Figure 7). Because the uncertainty in location of microseismic

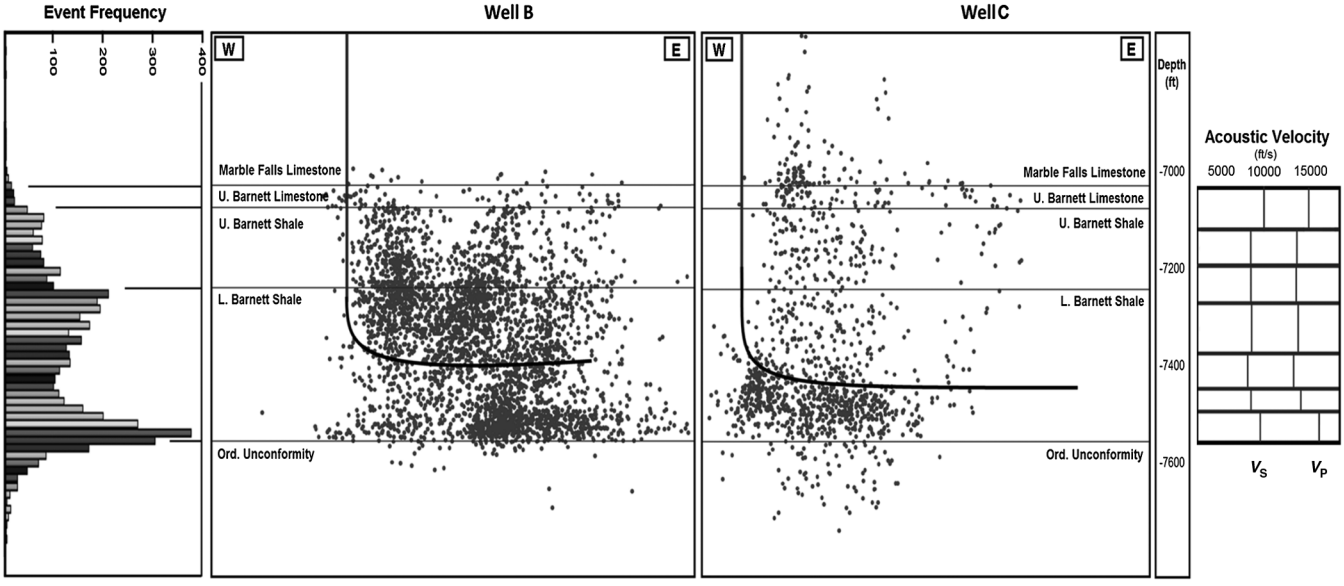

Figure 5. Side views from north and east of mapped microseismic events from wells B and C with simplified formation top surfaces. Horizontal lineaments in events cluster near formation boundaries.

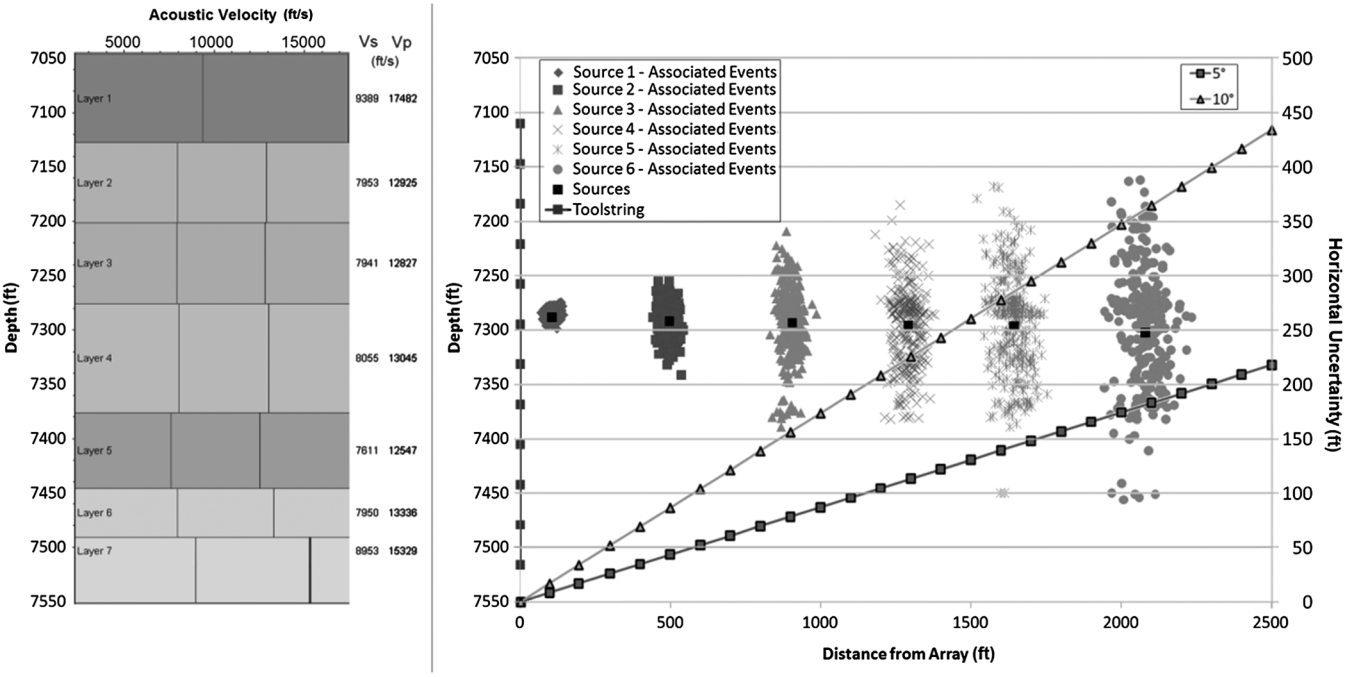

Figure 6. Plot of Monte Carlo analysis of 300 iterations of six different source locations associated with left depth axis. Each source location (black squares) has associated events, which increase in uncertainty linearly with distance. Our data set differs from this model in that most recorded microseismic events were located below the toolstring, increasing vertical scattering. Horizontal uncertainty from polarization analysis of first arrivals is associated with the right axis. The linearly increasing uncertainty is highest at 10° with an angular uncertainty of 131 m (430 ft).

events changes, we also analyzed the correlation of impedance to events within 366 m (~1200 ft) of monitoring wells (Figure 8a and 8b). These events should best represent the relationship of microseismic events to impedance values. In this restricted subset of the microseismic event data, events are still preferentially located within low impedance rocks for both Z_P and Z_S (approximately 65%–80%), and we conclude that the observed relationship between microseismic event locations and low seismic impedance is robust.

Our observation that fractures occur within rocks of low seismic impedance is consistent with the results of Rutledge and Phillips (2003), who find a correlation between shear activation of fractures and low seismic impedance, albeit in clastic units. However, our observation contradicts the general assumption that hydraulic stimulation preferentially fractures brittle rock to generate larger fracture systems and creates the most efficient drainage pathway (e.g., Grieser et al., 2007; Rickman et al., 2008). Gale et al. (2007) find that the tensile strength of the contact between the calcite fracture fill and the shale wall rock is low in the Barnett Shale, leading to a weak fracture-host boundary. We suggest that the low impedance zones preferentially fractured in our survey correspond to these calcite-cemented healed fractures, and that the induced fractures in our study area are reactivating existing fractures rather than breaking unfractured formation.

The distinct clustering of the microseismic events in low impedance rock suggests that, in our study area, rocks with particular seismic and material properties preferentially fail during hydraulic stimulation. These results imply that active seismic data may be utilized to identify subsurface zones of likely failure and potential reservoir drainage pathways.

Microseismic events, inverted Lamé parameters, and fluid properties

Low values of incompressibility λ and high rigidity μ appear to promote extensive induced fracture networks in gas shales (Goodway et al., 1997, 2010). These properties are also suggested to produce the lowest closure stresses, or largest individual fractures (Goodway et al., 1997). Rigidity μ determines the resistance to shear failure, and incompressibility λ is the resistance to fracture dilation, related to pore-pressure. In our results, low incompressibility and rigidity values in well A are characteristic of the Barnett Shale (Figure 9). In the bulk rock volume in well A (gray spectrum), where the stimulation included the Marble Falls Limestone and

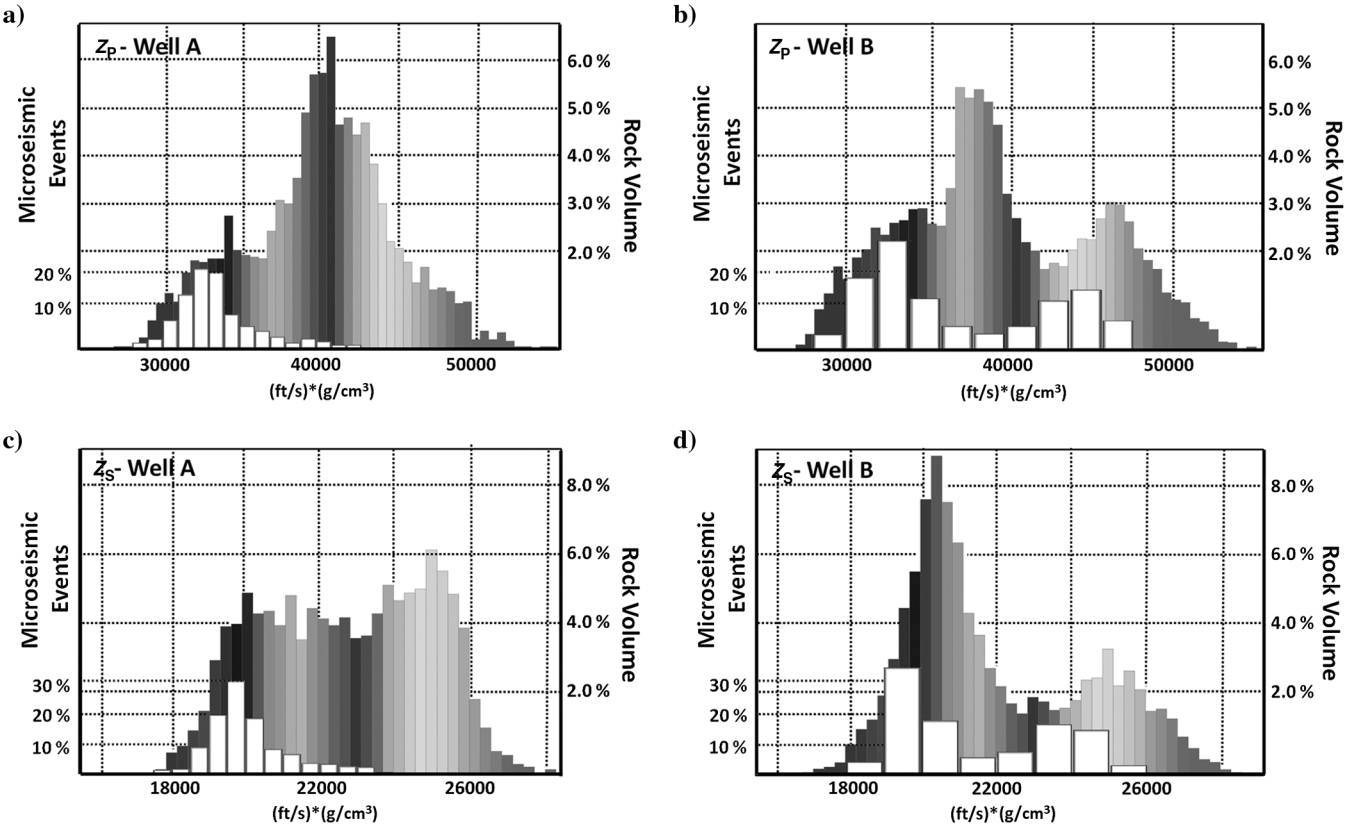

Figure 7. (a) Compressional-impedance values for the stimulated rock volume (grayscale histogram) compared to values within the stimulated rock volume in well A corresponding to microseismic event locations (white histogram). Note the correlation of microseismic event locations to lowest values of impedance. Well A is also representative of (b) well B, and wells C–D (not shown) for the relationship of event locations to P-impedance values. (c) Shear-impedance values of the stimulated rock volume (gray-scale histogram) compared to values within the stimulated volume corresponding to microseismic event locations (white histogram). Similar to P-impedance results, there is a correlation of microseismic event locations to lowest values of impedance in well A (and D, not shown). (d) Well B and well C (not shown), exhibit a bimodal behavior in S-impedance at microseismic locations, with events occurring within the lowest-impedance Barnett Shale and higher-impedance events within the overlying Marble Falls Limestone and underlying Ordovician carbonates.

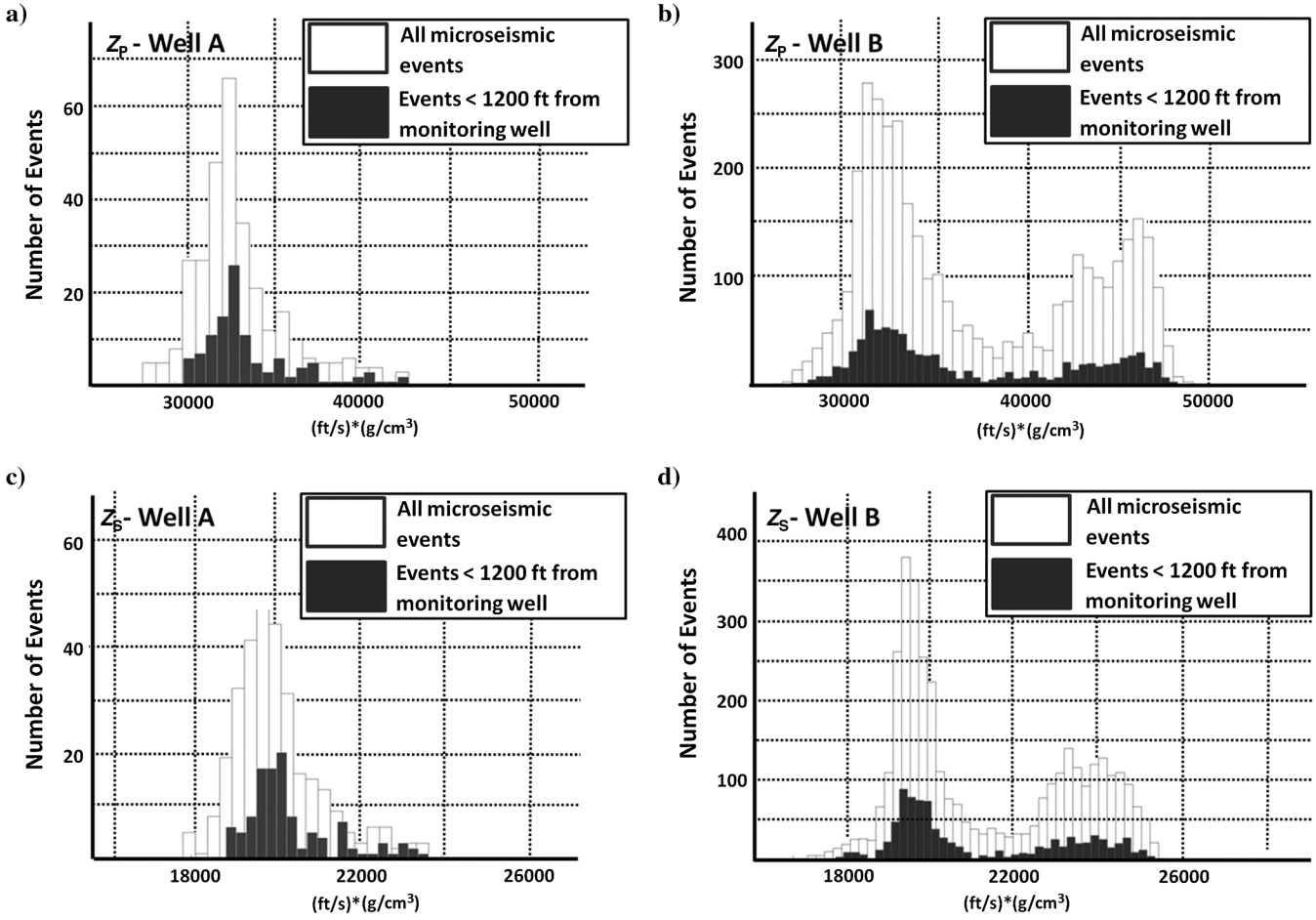

Figure 8. (a) Compressional-impedance values (Z_P) at all microseismic event locations for well A (white bars) and for only the subset of the events for well A located within 366 m (~1200 ft) of the monitoring well (black bars). The values of Z_P at event locations near the monitoring well mimic the range of Z_P values for the full distance range. (b) Values of Z_P at all microseismic event locations for well B (white bars) and for the subset of the events for well B located within 305 m (~1000 ft) of the monitoring well (black bars). Again, the values of Z_P at event locations near the monitoring well match the range of P-impedance values for events at all distances. The plots in (c) and (d) are similar, but show the S-impedance (Z_S) values for the full distance ranges (white bars) and the restricted ranges (black bars) for (c) well A and (d) well B. Similar to the ranges for Z_P, the ranges of values of Z_S at event locations near the monitoring wells are comparable to the ranges of Z_S values at event locations at any distance.

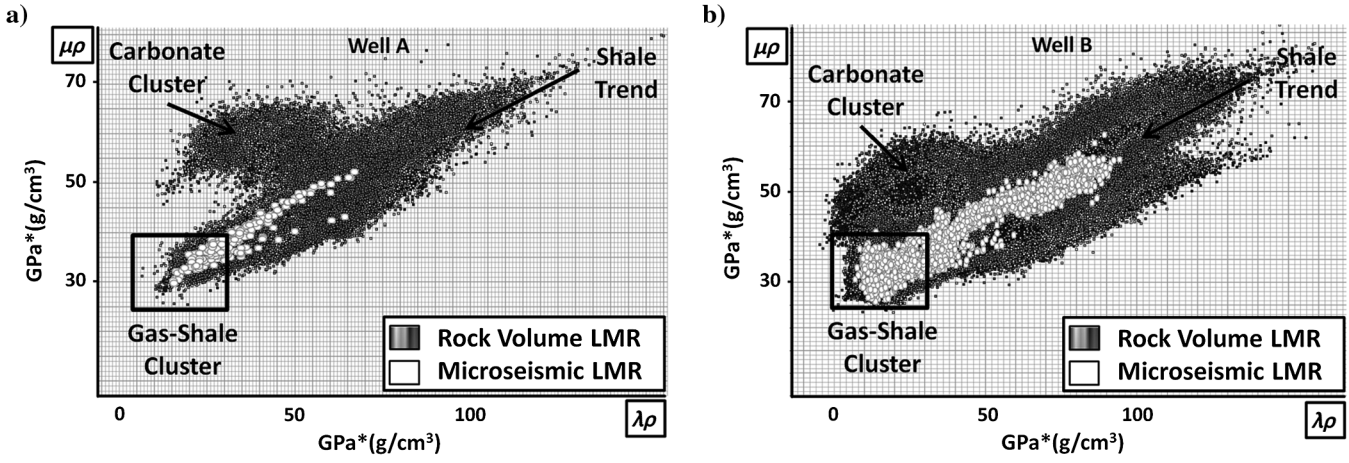

Figure 9. Crossplots of $\lambda\rho$ and $\mu\rho$ values of the rock volume (gray spectrum) and at the microseismic event locations (white). Squares define the potential gas-rich zones corresponding to low $\lambda\rho$ and $\mu\rho$ values, as defined by Aibaidula and McMechan (2009).

Ordovician carbonates, incompressibility and rigidity values cluster into two groups. The cluster of lower values of $\mu\rho$ corresponds to the Barnett Shale, and the grouping with high $\mu\rho$ values corresponds to carbonates. The fractured zones, white dots representing values at microseismic event locations, form a linear trend but dominantly have low values of $\mu\rho$ and fall within the Barnett Shale cluster, indicating that induced fracture systems in our region tend to occur in low incompressibility and low rigidity zones. The correlation between and microseismic event locations and low $\mu\rho$ was observed within both the full microseismic event data set and within the subset of the data restricted to events within 366 m (~1200 ft) of the monitoring wells. Because Lamé parameters are a function of impedance, the full event data set and events within 366 m (~1200 ft) are comparable to the impedance histograms observed in Figure 7. These results support the suggestion that active-source seismic properties can characterize zones of rock that are prone to failure during hydraulic stimulation.

For insight into the success of the stimulation program in these wells, we interpret gas-saturated zones from the $\mu\rho$ and $\lambda\rho$ values (Figure 9, boxes), and correlate with microseismic locations. Ideally, gas-saturated zones would be covered with microseismic events, and few would occur elsewhere. Gas-saturated V_P/V_S ratios are considered to be between 1.84–1.99 for limestone and between 1.7–3.0 for shale (Aibaidula and McMechan, 2009), and $\lambda\rho$ values are lower than $\mu\rho$ in gas-saturated units (Goodway et al., 1997). Using these assumptions, induced fractures interpreted from microseismic locations in well B have seismic property values consistent with gas-saturation. Conversely, well A shows V_P/V_S ratios of approximately 1.7 with $\lambda\rho$ greater than $\mu\rho$. This relationship may potentially explain the relative production history of these two wells; well B has higher production than well A, and the seismic properties identify greater gas-saturation of the shale near well B. However, the effectiveness of a stimulation program also depends on the viscosity of the stimulation fluid, the pressure applied during stimulation, and the duration of each stimulation stage. These parameters will impact stimulation effectiveness from well to well, but were unavailable for our investigation. Nevertheless, we see an intriguing correlation between production history and zones of interpreted gas-saturation and developed fractures, and suggest that this is a useful analysis for future surveys with well-located microseismic events.

Microseismic events and volumetric curvature

Past studies have found a correlation between microseismic event locations and volumetric curvature attributes, suggesting a tie between subsurface structures and preferred fracture paths (e.g., Mai et al., 2009; Guo et al., 2010; Thompson et al., 2010). In these studies, microseismic events dominantly cluster either within ridges/domes (Mai et al., 2009; Guo et al., 2010) or valleys/bowls (Thompson et al., 2010), but show a distinct preference in either case. In our study, we calculated long- and short-wavelength curvature, and characterized the structures within our seismic volume at microseismic event locations (Figures 2 and 10).

For the full microseismic data set, our results show an ambiguous relationship between microseismic event locations and structural features defined by curvature. In our short-wavelength curvature results, in well A 34% of microseismic events cluster in areas corresponding to structural domes and ridges, compared to 2% in bowl and valley structures, a result similar to the observations of Mai et al. (2009). In well B, 22% are in ridges and domes, compared to 16% in bowls or valleys (Figure 10a). Long-wavelength curvature plots for the full data set, however, do not show this same relationship. In well A, 28% of microseismic events line within bowl and valley structures, and the remainder lie in saddles. In well B, 19% are in ridges or domes, and 25% are in bowls or valleys (Figure 10b). The spread of events between bowls/valleys, saddles, and ridges/domes is substantial.

In subsets of the data set including only events near the monitoring wells, we see a stronger correlation between microseismic event locations with ridge and dome structures. In well A, for short-wavelength curvature at event locations within ~365 m of the monitoring well, 25% of events lie within ridges and domes, and none fall within bowls or valleys. For long-wavelength curvature using this restricted data set, virtually all events lie within saddles. The greater number of events associated with well B allow further spatial restriction, to within ~305 m of the monitoring well. In this subset, 34% of events lie within ridges or domes and 6% lie in bowls and valleys (short-wavelength), and 28% lie within ridges and domes and 13% lie in bowls and valleys (long-wavelength).

In all cases, however, most events lie within zones defined by curvature attributes as saddles. Unlike the previous studies (Mai et al., 2009; Guo et al., 2010; Thompson et al., 2010), there is no distinct clustering of microseismic events in ridges/domes or bowls/valleys. This lack of strong correlation may still reflect microseismic event location uncertainty as compared to the cells within which k_1 and k_2 were calculated, although we attempted to restrict distance to minimize the effect of location uncertainty. Alternatively, the spread may suggest a complex relationship between existing fractures and subsurface structural features.

DISCUSSION

Our prestack inversion of density and P- and S-impedance indicates that microseismic events fracture low density and low impedance rock. We suggest that the failure of low density and low impedance rocks represents the flow of stimulation fluids through weak, calcite-cemented fractures and faults. These calcite-cemented fractures and faults appear to be paths of least resistance within the Barnett Shale in our study area. Lamé parameters delineate the extent of the fracture systems into gas-bearing zones, and suggest that well B may be fracturing rock with higher gas saturation and thereby improving production results relative to well A.

Microseismic events in our study caused by hydraulic fracturing are directly correlated to the regional stress patterns in the Fort Worth Basin, mimicking primary faults at the large scale. At a smaller scale, microseismic events correlate to low impedance rocks, implying that complex fracture systems may be controlled by varying lithology or mineralogical content within the shale formation. Formation contact zones appear to act as barriers for propagating fracture systems; high-impedance formations like the Upper Barnett Limestone or the Ordovician Unconformity can act as fracture barriers, significantly helping to stimulate the formations between them. The formation contact zones are also possible planes of weakness and preferentially fracture during stimulation, although this observation may be biased by the strong velocity jump at the formation boundary and associated processing artifacts. Hydraulic fractures appear to predominately fracture rock within anticlinal 3D shapes (ridges and domes) or within saddles.

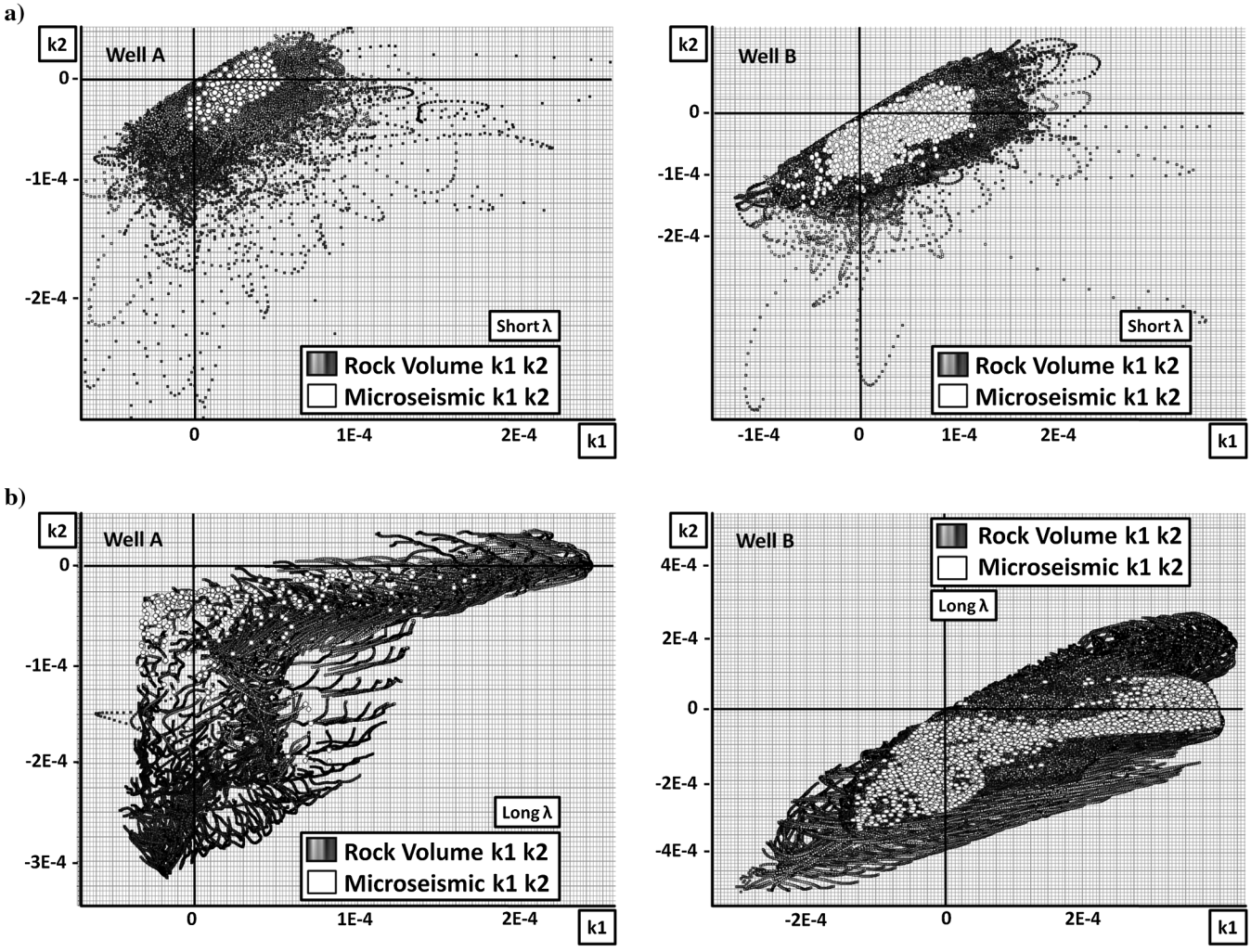

Figure 10. (a) Values of short-wavelength k_1 versus k_2 at microseismic event locations (white dots) and for the bulk rock volume surrounding events. In well A, 34% of microseismic events occur within ridge and dome structures, with 2% in bowl and valley structures. In well B, 22% are in ridges/domes, and 16% are in bowls/valleys. (b) Values of long-wavelength k_1 versus k_2 at microseismic event locations (white dots) and for the bulk rock volume surrounding events. In well A, 28% of microseismic events line within bowl and valley structures, and the remainder lie in saddles. In well B, 19% are in ridges/domes, and 25% are in bowls/valleys. For events located within 366 m (~1200 ft) of the monitoring well for well A and within 305 m (1000 ft) for well B, a greater percentage fall into ridge and dome structures, as described in the text. Units of k_1 and k_2 are theoretically 1/ft, the inverse of radius; however, structures are classified only by the sign and relative values of k_1 and k_2 and units are commonly omitted (e.g., Blumentritt et al., 2006). These events reflect all distances from the wellbore. Events close to the wellbore show a greater tendency to locate within ridges, domes, and saddles.

We find that fracture-prone rocks are consistently characterized by a specific range of values of seismic properties, including P- and S-impedance and Lamé parameters, suggesting that surface seismic properties can be indicative of zones of rock that are prone to failure during hydraulic stimulation. Based on these results, we suggest that active seismic data can provide a priori knowledge of preferred fracture system distribution, and may potentially be used for improved stimulation plans to target zones of interest more effectively. This may ultimately increase recovery rates from hydraulic stimulation.

CONCLUSIONS

We find that fracture-prone rocks are consistently characterized by a specific range of values of seismic properties, including P- and S-impedance and Lamé parameters, suggesting that surface seismic properties can be indicative of zones of rock that are prone to failure during hydraulic stimulation. Based on these results, we suggest that active seismic data can provide a priori knowledge of preferred fracture system distribution, and may potentially be used for improved stimulation plans to target zones of interest more effectively. This may ultimately increase recovery rates from hydraulic stimulation.

ACKNOWLEDGMENTS

We thank Devon Energy for providing data, financial support, and encouragement to undertake this study, along with Schlumberger and Hampson-Russell for providing licenses of Petrel and Strata to the University of Oklahoma for use in research and education. We

also thank Pinnacle for providing invaluable data and information. The authors would like to also acknowledge the editors, in particular L. Eisner, and three anonymous reviewers for their strong input, as well as Swift Energy for providing continuous support.

REFERENCES

Aibaidula, A., and G. McMechan, 2009, Inversion and interpretation of a 3D seismic data set from the Ouachita Mountains, Oklahoma: Geophysics, **74**, B37–B45, doi: 10.1190/1.3073005.

Aki, K., and P. G. Richards, 2002, Quantitative seismology, 2nd ed.: W. H. Freeman and Company.

Al-Dossary, S., and K. J. Marfurt, 2006, 3D volumetric multispectral estimates of reflector curvature and rotation: Geophysics, **71**, 41–51, doi: 10.1190/1.2242449.

Bardainne, T., and E. Gaucher, 2010, Constrained tomography of realistic velocity models in microseismic monitoring using calibration shots: Geophysical Prospecting, **58**, 739–753, doi: 10.1111/j.1365-2478.2010.00912.x.

Blumentritt, C. H., K. J. Marfurt, and E. C. Sullivan, 2006, Volume-based curvature computations illuminate fracture orientations — Early to mid-Paleozoic, central basin platform, west Texas: Geophysics, **71**, B159–B166, doi: 10.1190/1.2335581.

Bulant, P., L. Eisner, I. Pšenčík, and J. Le Calvez, 2007, Importance of borehole deviation surveys for monitoring of hydraulic fracturing treatments: Geophysical Prospecting, **55**, 891–899, doi: 10.1111/gpr.2007.55.issue-6.

Dufour, J., J. Squires, W. N. Goodway, A. Edmunds, and I. Shook, 2002, Integrated geological and geophysical interpretation case study, and Lamé rock parameter extractions using AVO analysis on the Blackfoot 3C-3D seismic data, southern Alberta, Canada: Geophysics, **67**, 27–37, doi: 10.1190/1.1451319.

Economides, M. J., and T. Martin, 2007, Modern fracturing: Enhancing natural gas production: ET Publishers.

Eisner, L., B. J. Hulsey, P. Duncan, D. Jurick, H. M. Werner, and W. Keller, 2010, Comparison of surface and borehole locations of induced seismicity: Geophysical Prospecting, **58**, 1365–2478.

Gale, J. F., R. M. Reed, and J. Holder, 2007, Natural fractures in the Barnett Shale and their importance for hydraulic fracture treatments: AAPG Bulletin, **91**, 603–622, doi: 10.1306/11010606061.

Goffey, R., 2009, AVO, inversion or AVO inversion? Hampson-Russell's software solutions: O&G Next Generation e-magazine, **9**, http://www.cisoilgas.com/article/AVO-inversion-or-AVO-inversion-Hampson-Russells-software-solutions/, accessed July 2010.

Goodway, B., T. Chen, and J. Downton, 1997, Improved AVO fluid detection and lithology discrimination using Lamé petrophysical parameters; "$\lambda\rho$","$\mu\rho$",&"λ/μ fluid stack", from P and S inversions: 67th Annual International Meeting, SEG, Expanded Abstracts, 183–186.

Goodway, B., M. Perez, J. Varsek, and C. Abaco, 2010, Seismic petrophysics and isotropic-anisotropic AVO methods for unconventional gas exploration: The Leading Edge, **29**, 1500–1508, doi: 10.1190/1.3525367.

Grieser, B., and J. Bray, 2007, Identification of production potential in unconventional reservoirs: Presented at the Production and Operations Symposium, Society of Petroleum Engineers.

Guo, Y., K. Zhang, and K. Marfurt, 2010, Seismic attribute illumination of Woodford Shale faults and fractures, Arkoma Basin, OK: 80th Annual International Meeting, SEG, Expanded Abstracts, **29**, 1372–1375.

Hampson, D. P., and B. H. Russell, 2005, Simultaneous inversion of pre-stack seismic data: 75th Annual International Meeting, SEG, Expanded Abstracts, 1633–1637.

Heidbach, O., M. Tingay, A. Barth, J. Reinecker, D. Kurfeß, and B. Müller, 2009, The World Stress Map based on the database release 2008, equatorial scale 1:46,000,000: Commission for the Geological Map of the World.

Jarvie, D. M., R. J. Hill, T. E. Ruble, and R. M. Pollastro, 2007, Unconventional shale-gas systems: The Mississippian Barnett Shale of north-central Texas as one model for thermogenic shale-gas assessment: AAPG Bulletin, **91**, 475–499, doi: 10.1306/12190606068.

Kidney, R. L., U. Zimmer, and N. Boroumand, 2010, Impact of distance-dependent location dispersion error on interpretation of microseismic event distributions: The Leading Edge, **29**, 284–289, doi: 10.1190/1.3353724.

Lisle, R. J., 1994, Detection of zones of abnormal strains in structures using Gaussian curvature analysis: AAPG Bulletin, **78**, 1811–1819.

Loucks, R., and S. T. Ruppel, 2007, Mississippian Barnett Shale: Lithofacies and depositional setting of a deep-water shale-gas succession in the Fort Worth Basin, Texas: AAPG Bulletin, **91**, 579–601, doi: 10.1306/11020606059.

Mai, H. T., K. J. Marfurt, and S. Chávez-Pérez, 2009, Coherence and volumetric curvatures and their spatial relationship to faults and folds, an example from Chicontepec basin, Mexico: 79th Annual International Meeting, SEG, Expanded Abstracts, 1063–1067.

Masaferro, J. L., M. Bulnes, J. Poblet, and M. Casson, 2003, Kinematic evolution and fracture prediction of the Valle Morado structure inferred from 3D seismic data, Salta province, northwest Argentina: AAPG Bulletin, **87**, 1083–1104, doi: 10.1306/02070301102.

Maxwell, S., 2009, Microseismic location uncertainty: CSEG Recorder, **34**, 41–46.

Miskimins, J., 2009, The importance of geophysical and petrophysical data integration for the hydraulic fracturing of unconventional reservoirs: The Leading Edge, **28**, 844–849, doi: 10.1190/1.3167787.

Pollastro, R. M., D. M. Jarvie, R. J. Hill, and C. W. Adams, 2007, Geologic framework of the Mississippian Barnett Shale, Barnet-Paleozoic total petroleum system, Bend arch-Fort Worth Basin, Texas: AAPG Bulletin, **91**, 405–436, doi: 10.1306/10300606008.

Rich, J. P., and M. Ammerman, 2010, Unconventional geophysics for unconventional plays: Presented at the SPE Unconventional Gas Conference, Society of Petroleum Engineers, 131779–MS.

Rickman, R., M. Mullen, E. Petre, B. Grieser, and D. Kundert, 2008, A practical use of shale petrophysics for stimulation design optimization: Presented at the 2008 Society of Petroleum Engineers Annual Technical Conference and Exhibition.

Roberts, A., 2001, Curvature attributes and their applications to 3D interpreted horizons: First Break, **19**, 85–100, doi: 10.1046/j.0263-5046.2001.00142.x.

Rothert, E., and S. A. Shapiro, 2003, Microseismic monitoring of borehole fluid injections: Data modeling and inversion for hydraulic properties of rocks: Geophysics, **68**, 685–689, doi: 10.1190/1.1567239.

Rutledge, J. T., and W. S. Phillips, 2003, Hydraulic stimulation of natural fractures as revealed by induced microearthquakes, Carthage Cotton Valley gas field, east Texas: Geophysics, **68**, 441–452, doi: 10.1190/1.1567212.

Shapiro, S. A., E. Rothert, V. Rath, and J. Rindschwentner, 2002, Characterization of fluid transport properties of reservoirs using induced microseismicity: Geophysics, **67**, 212–220, doi: 10.1190/1.1451597.

Thompson, A., J. Rich, and M. Ammerman, 2010, Fracture characterization through the use of azimuthally sectored attribute volumes: 80th Annual International Meeting, SEG Expanded Abstracts, **29**, 1433–1437.

Warpinski, N., 2009, Microseismic monitoring: Inside and out: Journal of Petroleum Technology, **11**, 80–85.

Zhang, K., B. Zhang, J. T. Kwiatkowski, and K. J. Marfurt, 2010, Seismic azimuthal impedance anisotropy in the Barnett Shale: 80th Annual International Meeting, SEG Expanded Abstracts, **29**, 273–277.

Zoback, M. D., and H.-P. Harjes, 1997, Injection-induced earthquakes and crustal stress at 9 km depth at the KTB deep drilling site, Germany: Journal of Geophysical Research, **102** (B8), 18477–18491, doi: 10.1029/96JB02814.